



CHORUS

This is the accepted manuscript made available via CHORUS. The article has been published as:

Topological Optical Waveguiding in Silicon and the Transition between Topological and Trivial Defect States

Andrea Blanco-Redondo, Imanol Andonegui, Matthew J. Collins, Gal Harari, Yaakov Lumer, Mikael C. Rechtsman, Benjamin J. Eggleton, and Mordechai Segev

Phys. Rev. Lett. **116**, 163901 — Published 20 April 2016

DOI: [10.1103/PhysRevLett.116.163901](https://doi.org/10.1103/PhysRevLett.116.163901)

Topological optical waveguiding in silicon and transition between topological and trivial defect states

Andrea Blanco-Redondo¹, Imanol Andonegui^{1,2}, Matthew J. Collins³, Gal Harari⁴, Yaakov Lumer⁴, Mikael C. Rechtsman³, Benjamin J. Eggleton¹, Mordechai Segev⁴

One-dimensional models with topological band structures represent a simple and versatile platform to demonstrate novel topological concepts. Here we experimentally study topologically protected states in silicon at the interface between two dimer chains with different Zak phase. Furthermore, we propose and demonstrate that, in a system where topological and trivial defect modes coexist, we can probe them independently. Tuning the configuration of the interface, we observe the transition between a single topological defect and a compound trivial defect state. These results provide a new paradigm for topologically protected waveguiding in a CMOS compatible platform and highlight the novel concept of isolating topological and trivial defect modes in the same system that can have important implications in topological physics.

Topological photonics [1] promises to provide robust transport of optical modes by suppressing backscattering, a major impediment to large-scale optical integration [2], slow-light applications [3], and quantum information processing [4] amongst others. Since the first theoretical proposal [5-7] and the first experimental demonstration of topologically protected electromagnetic propagation in the microwave regime [8], many proposals have been made to take topological concepts into the optical regime [9-12]. Experiments followed soon thereafter, demonstrating adiabatic pumping [13], and eventually photonic topological insulators [14,15]. Conceptually, the localized modes appearing at the interface of two structures with distinct topological invariants hold the promise to play a key role in the development of robust optical circuits. The simplest model to realize these so-called

¹Centre for Ultrahigh bandwidth Devices for Optical Systems (CUDOS), Institute of Photonics and Optical Science (IPOS), School of Physics, The University of Sydney, NSW 2006, Australia

²Departamento de Física Aplicada I, E.T.S. Ingeniería de Bilbao, Universidad del País Vasco (UPV/EHU), Alda. Urquijo s/n, 48013 Bilbao, Spain

³Department of Physics, The Pennsylvania State University, University Park, Pennsylvania 16802-6300, USA.

⁴Department of Physics, Technion - Israel Institute of Technology, Haifa 32000, Israel

*E-mail: andrea.blancoredondo@sydney.edu.au

photonic topological defect states in one dimension is the dimer chain (the so-called SSH model) [16]. This idea was demonstrated in optical experiments in 2009, on the edge of a binary waveguide array [17], and more recently in a non-hermitian system involving loss [18] and in a dimer chain of microwave resonators [19]. Analogous systems to the dimer chain have been recently proposed to demonstrate one-dimensional plasmonic and polaritonic topological edge states based on zigzag arrays of metallic nanoparticles [20], and micropillars [21]. Interestingly, ideas related to the SSH dimer chain were also recently explored, in the context of topological effects in one-dimensional quasicrystals, demonstrating Thouless pumping [22-24].

The theoretical understanding of the topological properties of the dimer chain was presented in [25] in the context of elucidating the existence of edge states in graphene ribbons. From the results in [25] it follows that interfacing two dimer chains with different Zak phase [26] gives rise to a topological transition and to the existence of a topologically protected defect state at the interface. The exact configuration of the waveguides around that interface determines the shape of the topological defect mode, and, in addition, it may give rise to the appearance of trivial defect states coexisting with the topological defect. These trivial defect modes are also localized at the interface. In general, this would give rise to beating between the trivial and topological defect modes leading to a compound defect mode.

In this Letter, we experimentally demonstrate that, counterintuitively, we can isolate the topological defect mode from the compound trivial defect mode and vice versa, even when the system supports both type of modes co-localized in the same region. The transition from the compound trivial state to a single topological defect is possible by varying the configuration of the waveguides at the interface between the two silicon waveguide dimer chains with different topological invariants. The realization that the topological defect mode can be probed separately to the trivial defect modes provides deeper understanding of the nature of topologically protected transport in photonic systems [5-8], and suggests that such phenomena are universal, that is, they should exist also in other physical systems, such as condensed matter physics [27] or atomic physics [28] – wherever topological and trivial states coexist. In addition to its fundamental interest, our physical setting represents a new platform for topologically protected waveguiding in silicon and opens the door to realizing optical circuits with immunity to fabrication imperfections or environmental changes in a CMOS compatible platform.

Here, we propose two potential configurations of a system comprising two dimer chains with different topological invariants, as shown in Fig. 1(a) and Fig. 1(b). It was shown in [25] that the ratio between the

hopping parameters between two elements in the same dimer, t' , and the hopping parameter between two dimers, t , determines the value of the Zak phase, $\mathcal{Z} = i \oint dq \langle u_q | \partial_q u_q \rangle$, where $|u_q\rangle$ are the Bloch wave functions [26]. In particular, $\mathcal{Z} = 0$ when $(t'/t) > 1$ and $\mathcal{Z} = \pi$ when $(t'/t) < 1$. The topological transition $(\mathcal{Z} = 0) \leftrightarrow (\mathcal{Z} = \pi)$ corresponds to the emergence of edge states, and \mathcal{Z} / π gives the number of topological states localized at the edge of each chain [25].

In Fig. 1(a) and Fig. 1(b) we interface a dimer chain with $(t'_a/t_a) > 1$, whose dimers are shaded in red, with a dimer chain with $(t'_b/t_b) < 1$, whose dimers are shaded in yellow. At the interface the inter- and intra-dimer hopping parameters are equal, i.e. $(t'/t) = 1$, and a topological transition $(\mathcal{Z} = \pi) \leftrightarrow (\mathcal{Z} = 0)$ occurs right at the interface. The connection between dimers can be arranged so that there is a *short-short* defect at the interface, as in Fig. 1 (a), or a *long-long* defect, as in Fig. 1 (b).

In coming to design our system – the photonic waveguide array – the separation between waveguides plays an important role. We chose the separation between waveguides such that the contrast between the intra- and inter-dimer hopping parameters is maximized, which guarantees a large band gap and in turn strong topological protection. However, certain practical issues restrict us. The minimum separation between waveguides is determined by the minimum feature size defined by the fabrication process, so as to avoid proximity effects. The maximum separation between waveguides is limited by the minimum spatial overlap between the individual waveguide modes, which defines the coupling coefficient between adjacent waveguides. In our experiment, it is very important that the propagation length in the waveguide array is large enough, at least 10 coupling lengths. With these considerations, we chose the proper parameters that ensure robust experimental observation of all the phenomena involved.

Consider first the particular case where each element of the dimer chains is a silicon waveguide of refractive index $n_{\text{Si}} = 3.48$ at 1550 nm, width $w = 450$ nm, height $h = 220$ nm, and length $L = 500$ μm . We fix the total number of waveguides to $n = 203$ and consider that the waveguides are separated by air ($n_{\text{air}} = 1$). For the short-short defect case we chose $d'_a = d_b = 182$ nm and $d_a = d'_b = 324$ nm, as the separation distances between waveguides. Using the silicon waveguide parameters above we obtain the coupling constants for each separation distance, and subsequently the hopping parameters. This yields $(t'_a / t_a) = 3.26$ and $(t'_b / t_b) = 0.31$. For the long-long defect case we chose $d'_a = d_b = 166$ nm and $d_a = d'_b = 294$ nm, giving the relations $(t'_a / t_a) = 2.96$ and $(t'_b / t_b) = 0.34$.

The transverse propagation constant at each waveguide for the short-short defect and the long-long cases is shown in Fig. 2 (a) and Fig. 2 (b), respectively. The band diagram in both cases is characterized by two bands separated by a band gap, as expected from one-dimensional dimer chains [25]. As a consequence of the defect, the topological transition occurs at the interface between the left and right dimer chains, and a topological defect state emerges in the middle of the band gap, as represented by the blue dots in Fig. 2 (a) and Fig. 2 (b). The transverse propagation constant of this topological defect is zero, which implies that the mode will remain exponentially localized at the interface, i.e. around waveguide number 0. The modal amplitudes of the topological defect mode across the nine central waveguides, for the short-short and long-long cases, are depicted by blue bars in Fig. 2 (c) and Fig. 2 (d) respectively. As anticipated, the configuration of the waveguides at the vicinity of the interface determines the shape of the defect mode. The short-short defect gives rise to an anti-symmetric modal amplitude with maxima in the odd waveguides and minima in the even waveguides, as shown in Fig. 2 (c), and the long-long defect generates the complementary defect state modal amplitude with maxima in the even waveguides and minima in the odd waveguides, as shown in Fig. 2 (d).

In addition to the topological defect state, the short-short defect case allows for two trivial defect states, represented by the red and green dots in Fig. 2 (a). These trivial defects appear because the short-short defect, formed by three waveguides closely spaced, constitutes a region of higher refractive index than the rest of the structure. Hence, as shown by the red and green bars in Fig. 2 (c), the power of the light populating these trivial defects is localized in the defect in the same spatial region as the topological defect. In this situation, the excitation (the input beam) determines the population of each mode and it can be used to isolate the topological mode from the compound trivial mode.

The two topological structures studied in Fig. 2 (a) and (b) are fabricated in a silicon-on-insulator (SoI) chip using deep-UV lithography at IMEC. To highlight the behavior of topological structures with respect to trivial structures, a third structure is fabricated: a coupled 1D waveguide array with equidistantly spaced silicon waveguides [29,30]. These three fabricated structures are depicted in Fig. 3 (a)-(c). The red and yellow waveguides in Fig. 3 (a) and (c) represent respectively the dimer chains with $(t_a/t_a') > 1$ and $(t_b/t_b') < 1$, similar to Fig. 1. The waveguides in Fig. 3 (b) are all blue to indicate that they are equidistantly spaced ($d_a = d_a' = d_b = d_b' = 230$ nm). Both the input and output waveguides have ten-degree grating couplers at their ends. We couple light (1550nm wavelength) into the structures by using an input waveguide that merges into waveguide number 0 of the arrays. To measure the light at the output, the nine central waveguides flare out at the output of the structures.

We first examine the underlying phenomena in simulations, which assume nearest-neighbor coupling. Under our parameters, any residual next-neighbor coupling is exceedingly small due to the tightly confined silicon modes. The simulations in Fig. 4 (a)-(c) show the propagation of that input signal across the 500 μm -long silicon waveguide structures represented in Fig. 3 (a)-(c) respectively. Note that only 120 waveguides are shown since virtually no power resides in the most external waveguides. Figure 4 (a) shows a characteristic beating pattern corresponding to the mix of the trivial defects. Throughout propagation, the power of this compound trivial defect remains localized around the short-short defect, in a recurrent fashion. The propagation behavior observed in the simulation of Fig. 4 (b) is explained by the well-known phenomenon of discrete diffraction [31, 32]. The light coupled into waveguide number 0 spreads as it propagates through the waveguide array, until at the output most of the power resides in two side-lobes far away from the center waveguide. These two side-lobes constitute the most distinct feature of diffraction in an equidistance waveguide array, a phenomenon known as “discrete diffraction” [31, 32], which is fundamentally different than diffraction in bulk systems (where most of the power remains in the center). The propagation simulation in Fig. 4 (c) shows a singular topological defect that propagates in the structure while always being exponentially localized around the defect.

We provide two different types of measurements to examine the propagation dynamics. First, to get a visual characterization of the power distribution at the output, we image the nine outputs of each structure using a 10x objective and a near-infrared (NIR) camera (Xenics Xeva 2785) set on a superior plane at an angle similar to the output angle of the grating couplers. The photographs in Fig. 4 (d)-(f) correspond to the output of the structures of Fig. 3 (a)-(c), respectively [33]. Second, to provide accurate measurements of the power distribution, we collect the light from each of the nine output grating couplers, using a fiber at a ten-degree angle, and measure it with a power meter. The normalized power extracted from these measurements is represented by blue bars in Fig. 4 (g)-(i), corresponding to the output of the structures in Fig. 3 (a)-(c) respectively. The grey bars in Fig. 4 (g)-(i) correspond to the propagation simulation results at the output, and show good agreement with the experimental measurements.

The measurements and simulations displayed in Fig. 4 (d) and (g) show a power maximum at the central waveguide, a zig zag intensity structure on either side with minima in the odd waveguides, and an exponential decay further away on both sides. This is the result of the beating between the two trivial defect modes, which yields a particular linear combination of the intensities of the two modes at each propagation distance. The output intensities are therefore extremely dependent on the length of the silicon waveguides. As illustrated by the simulation in Fig. 4 (a), 490 μm -long silicon waveguides (just 10 μm shorter than in the experiments) would

give rise to a very different output power distribution - with a local minimum in the central waveguide and maxima at the odd waveguides. Naturally, instead of varying the propagation distance, one can vary the wavelength which would scale accordingly. Hence, Fig. 5 shows measurements at different wavelengths to emulate various propagation lengths and so illustrate several linear combinations of interference (beating) between the trivial defect modes.

The measurements represented by the blue bars in Fig. 4 (h) show that, for the array with equidistant waveguides, very low power remains at the output facet of the nine central waveguides. This is because, as predicted from discrete diffraction [31,32] and from the simulations in Fig. 4 (b), most of the power resides in two side lobes around the waveguides number -60 and +60. Furthermore, there is a zigzag behavior observed in the measurements and simulations, and no monotonic decrease (away from the central waveguide) is observed, again consistent with discrete diffraction in an equidistant array. The experimental measurements and the simulations follow the same trends, although the quantitative agreement between them is not as good as in the structures with a topological defect. This is due to the fact that the fabrication imperfections significantly affect the optical transport in the extended structure experiencing discrete diffraction, whereas the topologically protected defect state propagates immune to them.

Finally, the measurements at the output of the long-long defect structure, represented by the image in Fig. 4 (f) and the blue bars in Fig. 4 (i), provide experimental proof of topologically protected waveguiding. The measurements show a single topological defect exponentially localized in the central waveguide, as predicted by the simulation (grey bars).

Altogether, the simulations and experimental measurements shown in Fig. 4 illustrate the transition from a compound trivial defect mode, composed by the mix of two co-localized trivial modes, to a single topological defect mode by simply tuning the configuration of the waveguides at the interface.

To demonstrate the beating behavior between trivial defects, we vary the wavelength across an 8 nm range around the central wavelength 1550 nm and study the output. Figures 5 (a)-(c) show the NIR camera images at the output of each of the three considered cases for five different input wavelengths. The images in Fig. 5 (a) show that varying the wavelength leads to different output power distributions, from having a maximum in the center and a zig-zag behavior with minimums in the odd waveguides for wavelengths of 1546 nm to 1550 nm, to a local minimum in the central waveguide at 1554 nm, passing through a maximum in the center with a monotonic decay for 1552 nm. Varying the wavelength causes a change on the coupling coefficient between adjacent waveguides and hence changes the beating period. It is therefore analogous to moving along the

propagation length and seeing the different power distributions shown in the simulation of Fig. 4 (a). Figure 5 (b) illustrates how discrete diffraction [31,32] is greatly influenced by the input wavelength, which determines the coupling length, and therefore different wavelengths lead to very different power distributions at the output. Finally, Fig. 5 (c) demonstrates that the topological defect mode maintains its power distribution at the output of the structure across the entire wavelength range.

In conclusion, the results presented here provided experimental evidence of topologically protected waveguiding in silicon. Further, we proved that transitioning from the compound trivial defect to a single topological defect is possible by tuning the defect configuration. By performing a wavelength dependent study we demonstrated waveguiding by a single topological defect in a silicon platform, as opposed to the discrete diffraction and beating by trivial modes. The experimental realization that one can independently probe colocalized topological and trivial modes could bring important fundamental implications to topological photonics and suggest similar phenomena in condensed matter systems and other physical systems – wherever topological and trivial states coexist. Further, this demonstration of topologically protected guiding of light at telecommunication wavelengths in silicon provides new ideas for developing CMOS-compatible devices immune to backscattering and environmental alterations. Likewise, among our future lines of work is studying the combined effects of topology and nonlinearity in these systems, exploring concepts similar to [34].

This work was supported by The University of Sydney and the Technion collaborative photonics research project funded by The Technion Society of Australia NSW and the NSW Department of Industry. The work was also founded by the Center of Excellence CUDOS (CE110001018) and Laureate Fellowship (FL120100029) schemes of the Australian Research Council (ARC). I. A. is supported by the Basque Country Government Saiotek (OPCOI) and the EHU/UPV PhD Fellowship 2012. M.C.R. acknowledges the support of the National Science Foundation under grant number ECCS-1509546.

References

1. L. Lu, J. D. Joannopoulos, and M. Soljačić, *Nature Phot.* **8**, 821 (2014).
2. F. Morichetti, A. Canciamilla, C. Ferrari, M. Torregiani, A. Melloni, and M. Martinelli, *Phys. Rev. Lett.* **104**, 033902 (2010).
3. A. Petrov, M. Krause, and M. Eich, *Opt. Express* **17**, 8676 (2009).
4. E. Knill, R. Laflamme, and G. J. Milburn, *Nature (London)* **409**, 46 (2000).
5. F. D. M. Haldane and S. Raghu, *Phys. Rev. Lett.* **100**, 013904 (2008).
6. S. Raghu and F. D. M. Haldane, *Phys. Rev. A* **78**, 033834 (2008).
7. Z. Wang, Y. D. Chong, J. D. Joannopoulos, and M. Soljačić, *Phys. Rev. Lett.* **100**, 013905 (2008).
8. Z. Wang, Y. Chong, J. D. Joannopoulos, and M. Soljačić, *Nature (London)* **461**, 772 (2009).
9. R. O. Umucalılar and I. Carusotto, *Phys. Rev. A* **84**, 043804 (2011).

10. M. Hafezi, E. A. Demler, M. D. Lukin, and J. M. Taylor, *Nature Phys.* **7**, 907 (2011).
11. K. Fang, Z. Yu, and S. Fan, *Nature Phot.* **6**, 782 (2012).
12. A. B. Khanikaev, S. Hossein Mousavi, W.-K. Tse, M. Kargarian, A. H. MacDonald, and G. Shvets, *Nature Mater.* **12**, 233 (2013).
13. Y. E. Kraus, Y. Lahini, Z. Ringel, M. Verbin, and O. Zilberberg, *Phys. Rev. Lett.* **109**, 106402 (2012).
14. M. C. Rechtsman, J. M. Zeuner, Y. Plotnik, Y. Lumer, D. Podolsky, F. Dreisow, S. Nolte, M. Segev, and A. Szameit, *Nature (London)* **296**, 196 (2013).
15. M. Hafezi, S. Mittal, J. Fan, A. Migdall, and J. M. Taylor, *Nature Phot.* **7**, 1001 (2013).
16. W. P. Su, J. R. Schrieffer, and A. J. Heeger, *Phys. Rev. Lett.* **42**, 1698 (1979).
17. N. Malkova, I. Hromada, X. Wang, G. Bryant, and Z. Chen, *Opt. Lett.* **34**, 1633 (2009).
18. J.M. Zeuner, M.C. Rechtsman, Y. Plotnik, Y. Lumer, S. Nolte, M.S. Rudner, M. Segev and A. Szameit, *Phys. Rev. Lett.* **115**, 040402 (2015).
19. C. Poli, M. Bellec, U. Kuhl, F. Montessagne, and H. Schomerus, *Nature Comm.* **6**, 7710 (2015).
20. A. P. Slobozhanyuk, A. N. Poddubny, A. Miroshnichenko, P. A. Belov, and Y. S. Kivshar, *Phys. Rev. Lett.* **114**, 123901 (2015).
21. D. D. Solnyshkov, A. V. Nalitov, and G. Malpuech, arXiv:1506.04626.
22. M. Verbin, O. Zilberberg, Y. E. Kraus, Y. Lahini, and Y. Silberberg, *Phys. Rev. Lett.* **110**, 076403 (2013).
23. M. Verbin, O. Zilberberg, Y. Lahini, Y. E. Kraus, and Y. Silberberg, *Phys. Rev. B* **91**, 064201 (2015).
24. The topological effects in quasicrystals are fundamentally different than those of the SSH dimer chain. Namely, the defect states embedded in the one-dimensional quasicrystal are not topological zero modes associated with the lattice. Rather, they are states that can be mapped to two-dimensional quantum Hall systems, which are protected in the two-dimensional space. Those states are not protected in any way in one dimension, unlike the topological defect observed this Letter (Figs. 2,4,5), which is topologically protected as an outgrowth of the SSH model.
25. D. Delplace, D. Ullmo, and G. Montambaux, *Phys. Rev. B.* **84**, 195452 (2011).
26. J. Zak, *Phys. Rev. Lett.* **62**, 2747 (1989).
27. Y. L. Chen, J. G. Analytis, J.-H. Chu, Z. K. Liu, S.-K. Mo, X. L. Qi, H. J. Zhang, D. H. Lu, X. Dai, Z. Fang, S. C. Zhang, I. R. Fisher, Z. Hussain and Z.-X. Shen, *Science* **325**, 178 (2009).
28. A. S. Sørensen, E. Demler, and M. D. Lukin, *Phys. Rev. Lett.* **94**, 086803 (2005).
29. A. L. Jones, *J. Opt. Soc. Am.* **55**, 261 (1965).
30. S. Somekh, E. Garmire, A. Yariv, H. L. Garvin, and R. G. Hunsperger, *Appl. Phys. Lett.* **22**, 46 (1973).
31. D. N. Christodoulides, F. Lederer, and Y. Silberberg, *Nature (London)* **424**, 817 (2003).
32. F. Lederer, G. I. Stegeman, D. N. Christodoulides, G. Assanto, M. Segev, and Y. Silberberg, *Phys. Rep.* **463**, 1 (2008).
33. The elongated tails at the left of each bright spot in Figs. 4(d-f) are an aberration caused by the ultra-high sensitivity of the NIR camera combined with the fact that it cannot be placed at exactly the same angle as the output of the grating couplers.
34. Y. Lumer, Y. Plotnik, M. C. Rechtsman, and M. Segev, *Phys. Rev. Lett.* **111**, 243905 (2013).

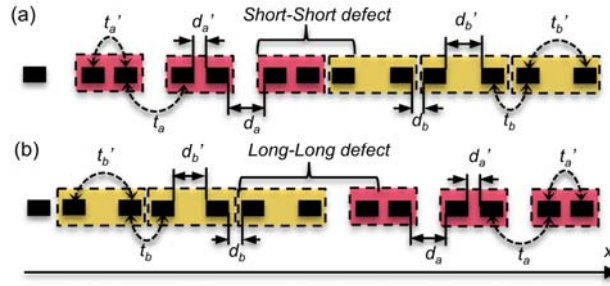


Fig. 1. Interfaces between dimer chains. (a) Two chains of dimers connect through a short-short defect. (b) Two chains of dimers connect through a long-long defect. The dimers shaded in red (resp. yellow) have an intra-dimer hopping parameter of t_a' (resp. t_b'), an inter-hopping parameter t_a (resp. t_b), and distances between waveguides of d_a and d_a' (resp. d_b and d_b'). Both structures present a topological transition, giving rise to a topological defect state at the interface. Additionally, the structure in (a) supports two trivial defect states.

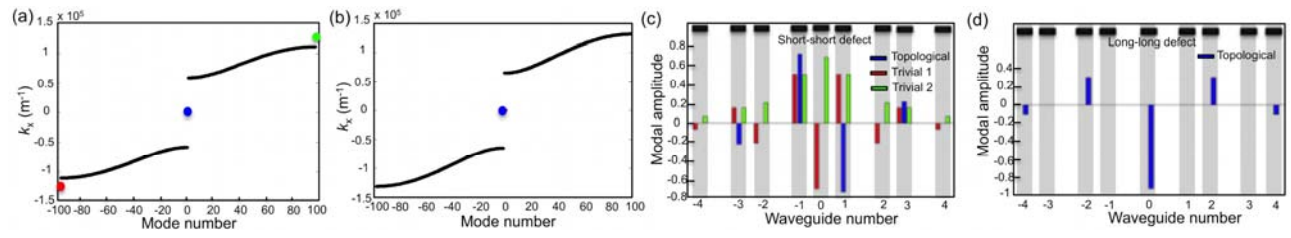


Fig. 2. Band diagrams and modal amplitudes around the defects. (a) Transverse propagation constant (k_x) of the modes at the short-short defect structure. The blue dot represents the topological defect mode, the red and green dots represent two trivial defect modes, the black curve represents the extended states; (b) k_x of the modes at the long-long defect structure. Only the topological defect and the extended states are supported by this system; (c) Modal amplitude of the topological (blue) and the two trivial defect modes (red and green) for the short-short defect case; (d) Modal amplitude of the topological defect mode for the long-long defect case.

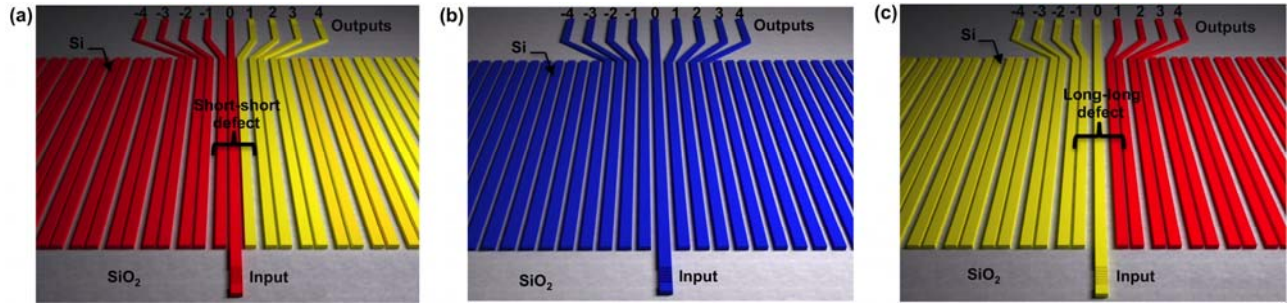


Fig. 3. Fabricated silicon-on-insulator structures. (a) Two silicon dimer chains connected by a short-short defect; (b) Array of equidistant coupled waveguides; (c) Two silicon dimer chains connected by a long-long defect. Each structure comprises 203 waveguides, with one input and nine outputs around the center. The red and yellow waveguides represent respectively the dimer chains with $(t_a/t_a) > 1$ and $(t_b/t_b) < 1$, whereas the waveguides in (b) are all equidistant to each other.

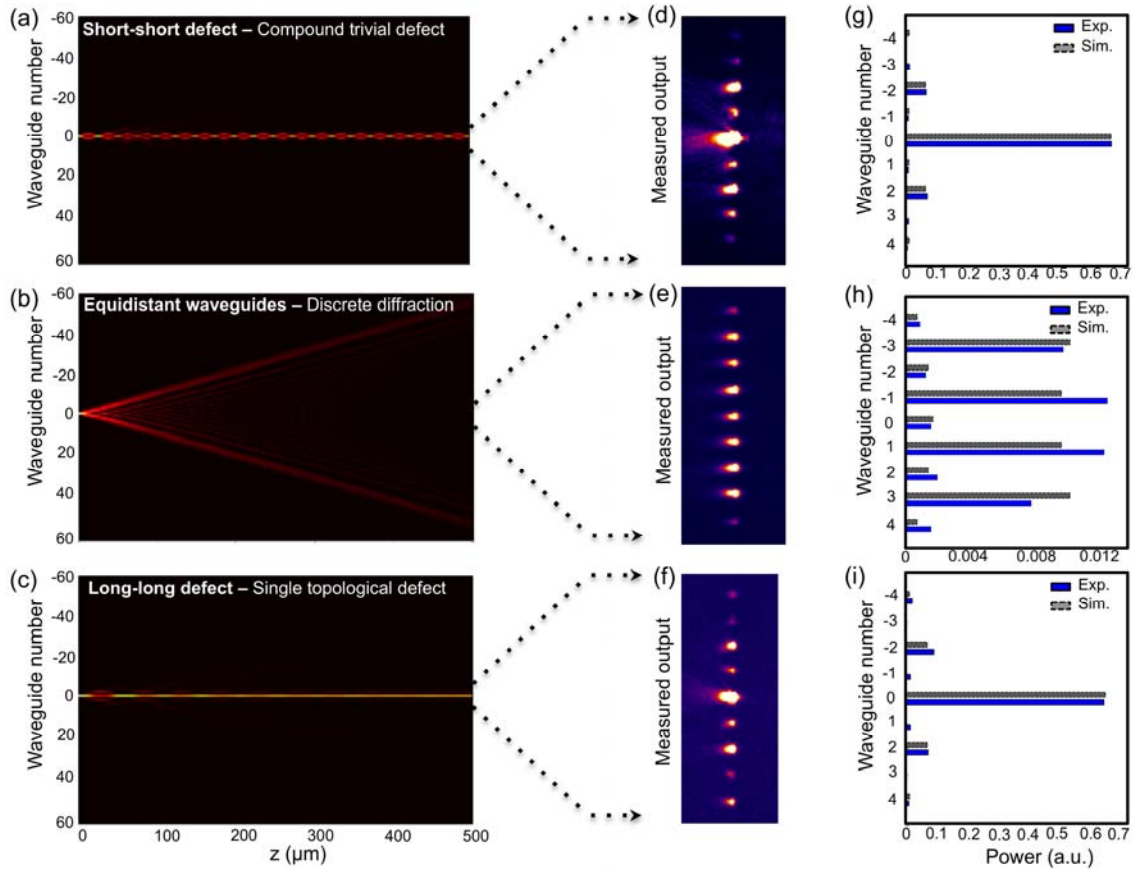


Fig. 4. Experimental and numerical results showing the transition from the guided trivial compound state to the guided topological defect state. (a)-(c) Propagation simulations of the input signal propagating through the structures of Fig. 3 (a-c) respectively; (d)-(f) NIR images at the output of the structures of Fig. 3 (a-c) respectively; (g)-(i) Power measurements (blue) and simulation results (grey) at the output of the structures of Fig. 3 (a-c) respectively.

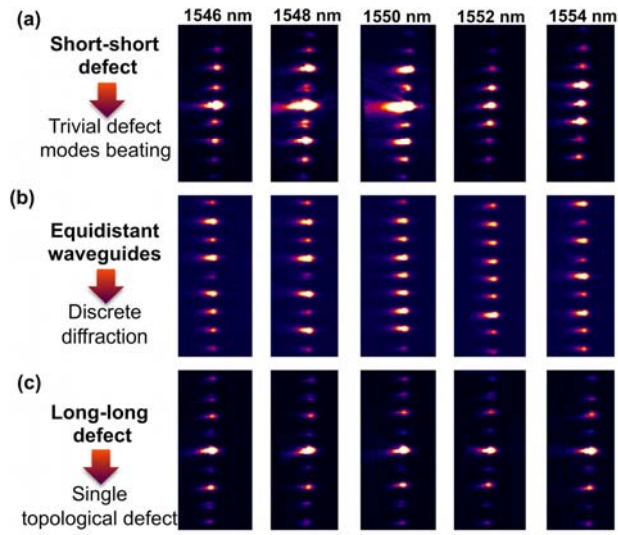


Fig. 5. Wavelength dependent behavior. NIR images at five wavelengths at the output of: (a) the short-short defect structure, illustrating beating between trivial modes; (b) the array of equidistant waveguides; (c) the long-long defect structure, illustrating the robustness of the topological defect to operational changes.